Microfabrication of piezoelectric MEMS based on thick $LiNbO_3$ single-crystal films

Merieme Ouhabaz[1], Djaffar Belharet[1], Quentin Micard[1], Mario Costanza[1], Giada Giuffrida[1], Ausrine Bartasyte[1,2], Carlo Trigona[3], and Samuel Margueron[1]

[1] FEMTO-ST Institute, University of Franche-Comté, CNRS (UMR 6174), ENSMM, 26 rue de l'Epitaphe, 25000 Besançon, France
[2] Institut Universitaire de France, Paris, France
[3] Dipartimento di Ingegneria Elettrica Elettronica e Informatica, Università degli Studi di Catania, viale A. Doria 6, 95125 Catania, Italy

E-mail: merieme.ouhabaz@femto-st.fr

Received xxxxxx
Accepted for publication xxxxxx
Published xxxxxx

Abstract

Microfabrication procedure of piezoelectric micro electro-mechanical systems based on 5 µm thick $LiNbO_3$ films on SiO_2/Si substrate at wafer scale including deep dry etching of thick $LiNbO_3$ films by implementing pulsed mode of Ar/SF_6 gas was developed. In particular, two (YXlt)/128°/90°$LiNbO_3$-Si cantilevers with tip mass were fabricated and characterized in terms of resonance frequency (511 Hz and 817 Hz), actuation and acceleration sensing capabilities. The quality factor of 89.5 and the electromechanical coupling of 4.8 % were estimated from measured frequency dependency of electrical impedance, fitted by using BVD model. The fabricated piezoelectric MEMS have demonstrated highly linear displacement with good sensitivity (5.28±0.02 µm/V) as a function of applied voltage and high sensitivity to vibrations of 667 mV/g indicating a suitability of the structure for actuation purposes and for acceleration or frequency sensing with high precision, respectively.

Keywords: piezo-MEMS, $LiNbO_3$, pulsed plasma etching, micro actuators, accelerometric sensor

1. Introduction

Piezoelectric micro-electro-mechanical systems (piezo-MEMS) are of special interest for a variety of applications ranging from biological microdevices, printer heads, integrated microphones, microactuators, acoustic filters, sensors, energy harvesters, etc. 1. Furthermore, the continuously increasing use of electronic devices requires urgently to find environment-friendly sensors and transducers. In the state-of-the-art of the piezo-MEMS, most of the attention has been devoted to piezoelectric thin films of lead-based materials such as $PbZr_{1-x}Ti_xO_3$ (PZT) 2 or lead-free piezoelectrics ($KNbO_3$, $BaTiO_3$, AlN, $Al_{1-x}Sc_xN$, ZnO, etc.) 3, deposited by physical or chemical deposition methods. Lead based materials are known for their good piezoelectric properties, PZT is one of most used material, it has a high electromechanical transduction efficiency. It can be found at industrial scale as ceramics or thin films, deposited mainly by sputtering and sol-gel methods. However, Pb-based materials represent an environmental issue and do not respect REACH and RoHS regulations in EU. The fabrication maturity of ZnO and AlN films and its compatibility with the conventional integrated circuit technology makes these materials an interesting alternative to Pb-based materials for piezo-MEMS applications. AlN thin films are used for the fabrication of bulk acoustic wave (BAW) filters and $Al_{1-x}Sc_xN$ films, offering higher electromechanical coupling than AlN, are considered for the next-generation filters. However, AlN and ZnO present relatively low electromechanical coupling in comparison to that of the Pb-based materials. (K,Na)NbO_3

(KNN) thin films are considered as one of the most promising materials for the replacement of PZT in piezo-MEMS [4]. Recently, high-quality KNN thin films with piezoelectric properties comparable to those of PZT at wafer scale were reported [5]. $LiNbO_3$ single crystals is a well-known material for photonic and micro-acoustic applications in telecommunication industry. $LiNbO_3$ thin films were not considered for the industrial applications in the fields of acoustics and photonics due to difficulties to obtain grown films with acceptable physical properties [6] until the development of ion-slicing [7] and bonding-polishing methods of these films [8-10]. These technologies allow to access single-crystalline-quality $LiNbO_3$ films with thicknesses in the range of 300-900 nm and above 1 µm, respectively. $LiNbO_3$ wafer bonding and lapping/polishing allows to access not only thick $LiNbO_3$ films in the range of few microns to full wafer thickness but also a moderate price for fabrication of custom heterostructures. It was demonstrated that (YXlt)/128°/90° $LiNbO_3$ orientation presents an electromechanical coupling as good as PZT in bending mode and possibility to harvest vibrational energy at low frequencies and meso-scale with the same high-efficiency as that of PZT-based harvesters [8,11]. Moreover, the high Curie temperature of about 1170°C makes $LiNbO_3$ of particular interest for the actuators, sensors, harvesters operating in harsh environment. Further developments of electro-active devices based on $LiNbO_3$ such as actuators, sensors or harvesters at MEMS scale need to be explored.

However, $LiNbO_3$ is highly chemically inert material at ambient conditions, and this makes wet and dry etching of $LiNbO_3$ difficult [12,13]. Hui and al. fabricated ridge waveguides by combining chemical and physical etching. A mixture of HF, HNO_3 and ethanol was used to etch 7.7 µm depth, and to fabricate the interdigital lamellas with 2.6 µm width and 2.8 µm separation. To improve the anisotropy, they used fluorine plasma etching in continuous-wave (CW) facing the redeposition of LiF, which causes lowering the etching rate and necessity to repeat cleaning and etching processes several times [14]. The wet etching of $LiNbO_3$, based on HF solutions, is highly anisotropic [15], very slow process, difficult to control and to make selective with respect to other stack materials. Therefore, mainly dry etching techniques and in particular physical etching are considered for the fabrication of optical micro-guides with etching rate of 30 nm/min [16]. Moreover, the dry etching remains limited to the sub-micron depths. Consequently, the fabrication of MEMS based on thick lithium niobate films and SiO_2/Si substrate is still challenging and requires development of specific deep dry etching methods. For instance, Aryal et al. used proton exchanged $LiNbO_3$ to prevent LiF formation and its redeposition [17].

In this paper, we report a microfabrication of piezo-MEMS based on 5 µm thick $LiNbO_3$ films on SiO_2/Si substrate. A pulsed dry etching technique using Ar/SF_6 gas was developed for this purpose. The fabricated $LiNbO_3$-Si cantilevers with tip mass were characterized in terms of resonance frequency, actuation and acceleration sensing capabilities. The experimental results were supported by finite element simulation.

2. Microfabrication process

In this work, two clamped cantilevers (A/B) with the width of 0.6 mm / 1mm and the length of 6.7 mm / 7 mm, based on piezoelectric (YXlt)/128°/90° (hereafter 128°Y-Z') $LiNbO_3$ single crystalline film with thickness of 5 µm, 37 µm Si and the tip mass of 2 mm / 1.9 mm, was considered (the A cantilever is illustrated in Figure 1). The parallel plate system Au electrode system was implemented.

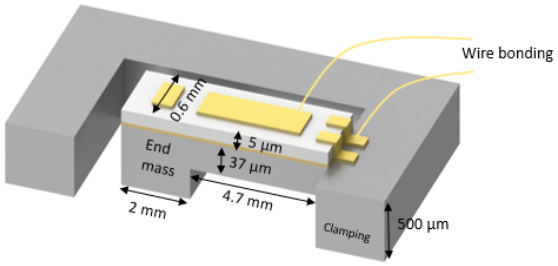

Figure 1. Schematical representation of the geometrical dimensions (in mm) of the A cantilever with tip mass, based on $LiNbO_3$ (5µm) and Si.

A flowchart of the fabrication process of $LiNbO_3$ based MEMS is presented in Figure 2. The first step was the Au-Au thermocompression bonding of a 350 µm thick 128°Y-Z' $LiNbO_3$ wafer on a 536 µm thick Si wafer with 1.2 µm thick SiO_2 by using wafer bonder EVG501 (Figure 2 a). For this purpose, 150 nm Au layer with 25 nm Cr adhesion layer were sputtered on both substrates, then a uniaxial pressure was applied to bring together the gold films to atomic distance. The bonding process was done at room temperature to avoid thermal stresses and pyroelectric charges which could damage $LiNbO_3$ crystal. After bonding step, the $LiNbO_3$ is thinned down to thickness of 5 µm by means of mechanical lapping and polishing processes (Figure 2 b). Then, a 5.6 µm thick Ni hard mask, deposited by electroplating on a sputtered (15 nm)Ti/(150 nm)Cu layers, was patterned on the $LiNbO_3$ surface (Figure 2 c). The reactive ion etching was done by using Corial RIE-CCP. Different etching parameters were used for the Cu, Ti and $LiNbO_3$ layers. The Cu layer was etched by using an Ar^+ plasma at room temperature (20 °C). The RF power was 200 W, the chamber pressure - 10 mTorr, and Ar flow - 100 sccm. A fluorinated chemistry was used to etch Ti layer by using C_2F_6/O_2/Ar (50/20/2 sccm) gas and the RF power of 150 W (Figure 2 d).

After etching the Ti/Cu layers, $LiNbO_3$ etching was done by using the RF power of 200 W, the chamber pressure of 15 mTorr, the temperature of 20°C, and the SF_6 /Ar gas ratio of

50/50 sccm (Figure 2 e). For shallow etching (etching depth < 1 µm), the continuous mode can be used and allows attain acceptable etching rate and roughness of etched surfaces. For the deep etching, a strong roughness of etched walls was observed (Figure 3). This roughness can be attributed to the re-deposition of the used metal hard mask but also to the non-volatile reaction products. This limits the etching depth by means of continuous SF_6 /Ar etching.

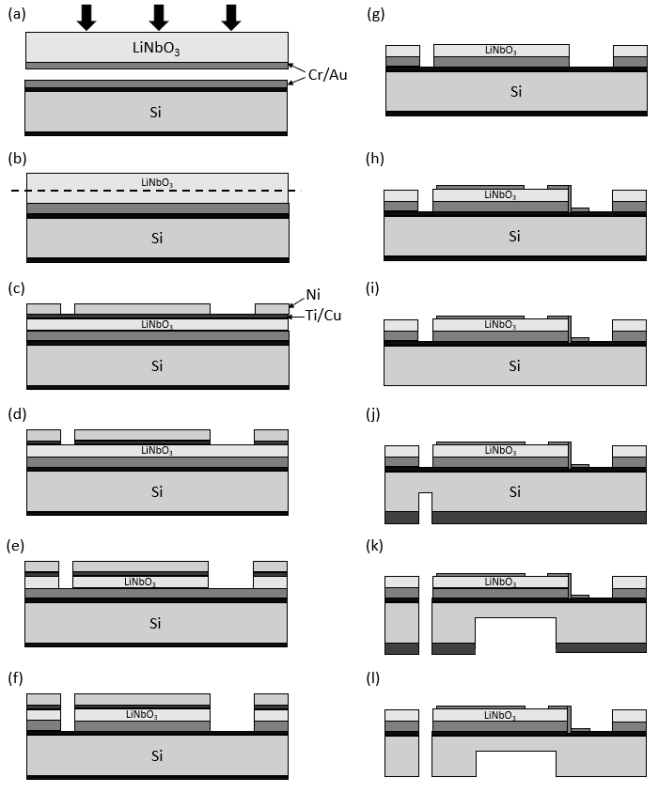

Figure 2. Flow chart of the fabrication process of $LiNbO_3$-Si based MEMS: gold bonding of $LiNbO_3$ and Si wafers (a), $LiNbO_3$ lapping and polishing (b), sputtering of Ti/Cu and structuring of Ni hard mask, grown by electroplating (c), Ti/Cu plasma etching (d), $LiNbO_3$ plasma etching (e), Cr/Au/Cr plasma etching (f), hard mask stripping using chemical etching (g), top electrode deposition on $LiNbO_3$ (h), SiO_2 etching by HF solution (i), photolithography and 1st plasma etching of Si (j), photolithography and 2nd plasma etching of Si (k), final cantilever structure based on $LiNbO_3$ on Si (l).

To overcome these issues, a new process with pulsed gas flow as a function of time was developed. Meanwhile, pulsed mode of RF power input offers promising way to expand the range of operating conditions [18,19] for MEMS and MOS technologies. Usually, two main parameters characterize the RF pulse: pulse duty cycle and pulse frequency. The latter is defined as the ratio between the pulse ON time and the total pulse sequence time. By varying the pulse frequency and the duty cycle, pulsed plasmas provide additional "control knobs" in which primary plasma properties, such as electron temperature, ion/neutral flux ratio, ion/electron densities, and plasma potential, can be controlled [20,21]. Pulsed ICP reactors contributes to minimize plasma induced damage. It was reported that reduced damage is due to charging effects [22-24], reduced surface damage [25,26], reduced ion energies [27-29], reduced UV damage [30,31], increased plasma uniformity [32,33] and an increased selectivity [19, 34]. In the case of $LiNbO_3$, the first sequence of the etching is based on an etching with SF_6/Ar gas like in the continuous mode. In the second sequence, the SF_6 flow is disabled and only the Ar^+ etching is used (Figure 4), which helps to remove the re-deposited hard metal mask and non-volatile by-products in the bottom of the trenches. The etched depth is no longer limited by the redeposited matter, and it only depends on the thickness of the hard mask used.

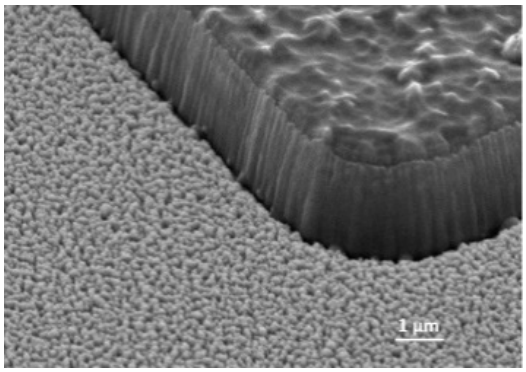

Figure 3. SEM image of the etched sidewall in LiNbO3 by using continuous SF6 /Ar^+ etching.

The Cr/Au layers, used for bonding process, are used as a detection layer for the end of $LiNbO_3$ etching by means of optical emission spectroscopy. After verifying the complete etching of $LiNbO_3$ over the entire wafer surface, another etching process was done to etch the Cr/Au layers by using Ar^+ plasma (RF power of 200 W, the chamber pressure of 10 mTorr, the temperature of 20 °C, and the Ar flow of 100 sccm), which allows to remove the two layers by a physical sputtering effect (Figure 2 f). The etching rate of Ni mask was 3 nm/min and that of $LiNbO_3$ – 28 nm/min, resulting in selectivity of 9. The remaining Ni/Cu/Ti hard mask was removed using wet etching process and the wafer was cleaned using RCA bath (H_2O, H_2O_2, NH_4OH) in order to remove all the defects, present on the walls and the bottom trenches (Figure 2 g). A lift-off process was then used to structure the top Cr/Au electrode, deposited by sputtering (Figure 2 h).

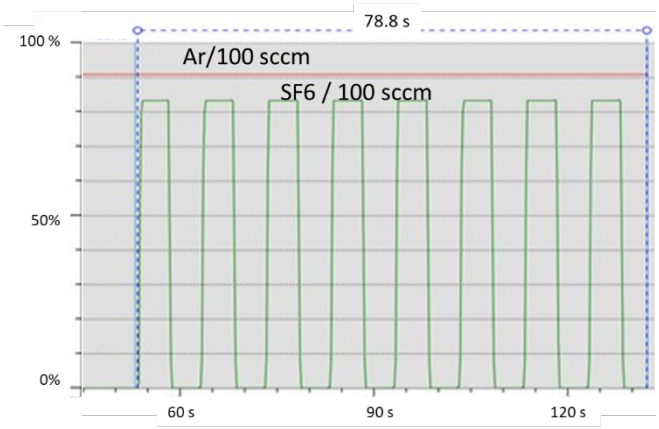

Figure 4. Continuous Ar and sequenced SF_6 gas flows during pulsed reactive ion etching of $LiNbO_3$.

Afterwards, the wafer was structured on the silicon side. First, the 1.2 µm SiO_2 was removed from the Si surface using HF solution (Figure 2 i) and AZ40XT resist with thickness of 6 µm was patterned on the Si surface by means of UV lithography. For the silicon etching, pulsed mode was used, and the process parameter concerned by the pulsing was the RF power. In order to achieve deep silicon/SOI wafers the Bosch process [35,36] is the most used in the MEMS/MOEMS and piezo-MEMS technologies. This process consists of the cyclic isotropic etching and fluorocarbon-based protection film deposition by gas switching. The SF_6 plasma cycle etches silicon, and the C_4F_8 plasma cycle creates a protection layer. Therefore, The Bosch process using deep reactive ion etching (DRIE, SPTS), based on the repetition of 3 steps (C_4F_8 deposition, etching of polymer by SF_6, and isotropic etching by using SF_6) was implemented for Si etching in this work, as well [37]. Optical emission spectroscopy (OES), based on the light emitted from the plasma during etching processes, was used to detect by-products. When the etching is completed, the plasma chemistry changes, and detection of this difference indicates the end-point. First, the depth of 100 µm in the Si wafer was etched (Figure 2 j) and then the second photoresist mask was patterned, and the same etching process was repeated to release completely the structures (Figure 2 k). Figure 5 shows the final edge of $LiNbO_3$ single crystalline film on silicon after complete Si etching. The verticality of the $LiNbO_3$ walls was of 69.5°. Finally, the wafer was cut into separate devices by using femtosecond laser, which were wire bonded to a gold printed circuit board (Figure 5).

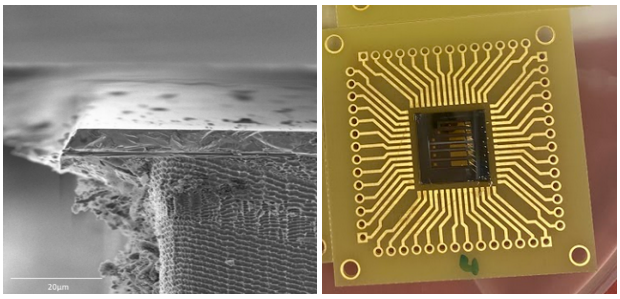

Figure 5. SEM image of $LiNbO_3$-Si based MEMS after the Bosch process (left) and photo of $LiNbO_3$-Si MEMS cantilevers wire bonded on printed circuit board (right).

3. Electro-mechanical characterization

The electrical impedance of fabricated $LiNbO_3$-Si transducer (A cantilever, its geometrical parameters are defined in Figure 1) was characterised using a network analyser, Bode100 (Omicron Lab, Austria) with a resistive bridge calibrated at 1 kΩ. The data was acquired from 450 Hz to 600 Hz at room temperature and interpolated using a Butterworth Van-Dyke (BVD) equivalent circuit (Figure 6). The electrical parameters of the electrical circuit were extracted: the inductance, L, of 11.188 kH, the capacitance, C, of 8.71 pF, the resistance, R, of 405 kΩ, and the parallel plate capacitor, C_0, 170.93 pF. The series and parallel resonant frequencies, f_s and f_p respectively, mechanical quality factor, Q, and electromechanical coupling factor, K^2_{eff}, of the transducer were calculated using these equations:

$$f_s = \frac{1}{2\pi}\sqrt{\frac{1}{LC}}, \quad (1)$$

$$f_p = f_s\sqrt{1+\frac{C}{C_0}}, \quad (2)$$

$$Q = \frac{2\pi}{f_s RC}, \quad (3)$$

$$K^2_{eff} = \frac{f_p^2 - f_s^2}{f_p^2}. \quad (4)$$

The f_s of 509.8 Hz, f_p of 535.8 Hz, Q factor of 89.5, and the electromechanical coupling, K^2_{eff}, of 4.8 % were estimated from BVD equivalent circuit fitting data.

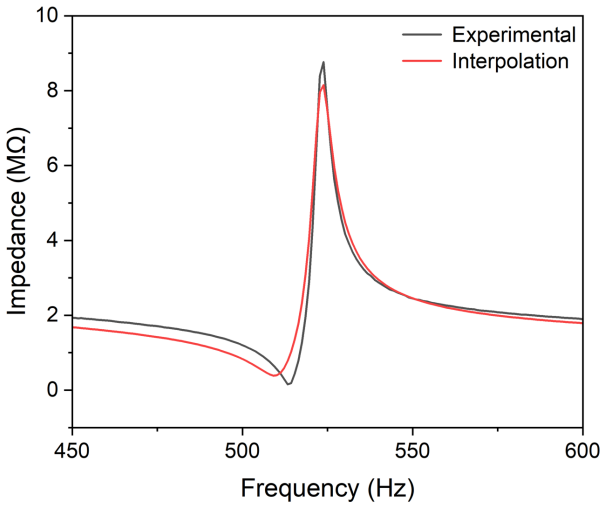

Figure 6. Experimentally measured impedance of fabricated $LiNbO_3$-Si transducer (A cantilever) as a function of frequency, and its fitting by using BVD model.

The mechanical displacement under electrical excitation at resonance frequency was measured by using MSA-100-3D Micro System Analyzer (Polytec GmbH, Germany). An amplitude of 22 µm was measured at 4 V_{RMS} (root mean square) in resonance mode at 511 Hz as shown in Figure 7. The resonance frequency and the maximum displacement, measured experimentally, are in a good agreement with the simulations done by COMSOL Multiphysics (USA) using the geometrical parameters of the cantilever (Figure 1) and the elastic properties of silicon and $LiNbO_3$. At resonance frequency, the displacement amplitude of about 30 µm was simulated for the excitation voltage of 4 V (Figure 7).

Figure 8 shows the mechanical displacement and quality factor of the first cantilever (Figure 1) measured at resonance frequency (511 Hz) as a function of excitation voltage. One can note the high linearity of displacement with efficiency of 5.28±0.02 µm/V for the actuation voltage range 0 - 5 V. The studied cantilever broke at V_{RMS} > 5 V indicating the limit of the elastic regime. Meantime, the quality factor reduced from 507 at voltage of 0 V to 474 at 5 V. The non-linearity of the quality factor indicates probably a higher order viscous term that can probably be due to air friction.

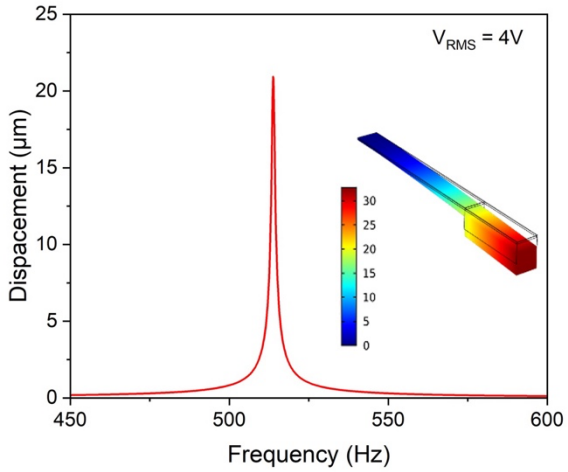

Figure 7. Frequency dependence of mechanical displacement of fabricated $LiNbO_3$-Si cantilever (A) under excitation voltage, V_{RMS}, of 4 V. Simulated deflection of the cantilever with the equivalent geometrical parameters (as defined in Figure 1) and under the same excitation voltage is given in the inset.

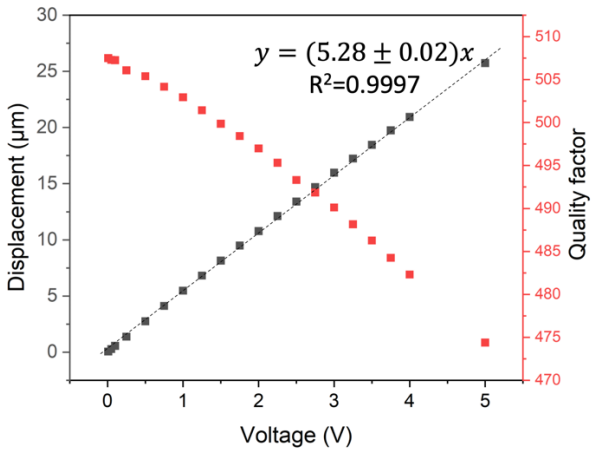

Figure 8. Displacement amplitude and quality factor of $LiNbO_3$-Si cantilever with tip mass (A cantilever with geometrical parameters given in Figure 1) as a function of actuation voltage at resonance frequency of 511 Hz.

A new beam with tip mass with width of 1 mm, length of 7 mm and tip mass of 1.9 mm, consisting of 5 µm thick $LiNbO_3$ on 37 µm thick Si wafer (B cantilever), was used for the accelerometric sensor calibration. The characterisation setup was composed of the beam clamped on a shaker, an accelerometer, a function generator with power amplifier and an oscilloscope with 10 MΩ (x10) impedance. The output voltage was measured at different acceleration values from 0.15 g to 0.6 g, as shown in Figure 9. The resonance frequency, estimated from maximum voltage response, was 818 Hz and 820 Hz at acceleration of 0.15 g and 0.6 g, respectively. The frequency dependence of generated voltage was asymmetric with respect to the resonance frequency and these nonlinearities were dependent on the acceleration

amplitude. Moreover, the hysteresis during frequency sweeping up (from low to high frequency) and sweeping down (from high to low frequency) was observed (Figure 10). Such nonlinearities are commonly observed in piezoelectric responses [38]. The nonlinearity and hysteresis can be attributed to friction, but also to damping [38] and to higher harmonic mode coupling [40]. The $LiNbO_3$-Si transducer could be considered as a sensor of low accelerations up to 0.58 g with the linear relationship between the generated voltage and the acceleration of 667.1 ± 7.9 mV/g (Figure 11).

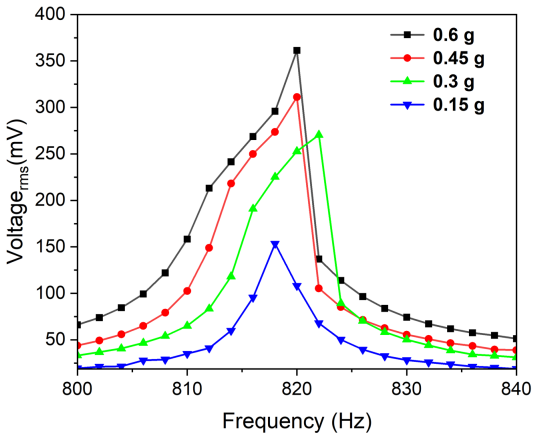

Figure 9. Generated voltage by $LiNbO_3$-Si cantilever (B) as a function of mechanical excitation frequency at various acceleration amplitudes (frequency sweep up).

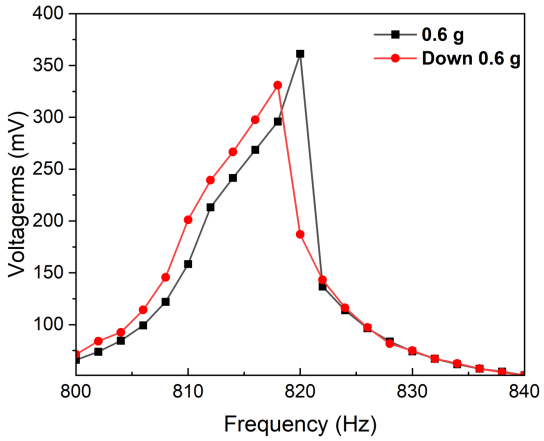

Figure 10. Voltage response of the $LiNbO_3$-Si cantilever (B) with tip mass as a function of frequency sweeping up and down at acceleration of 0.6 g.

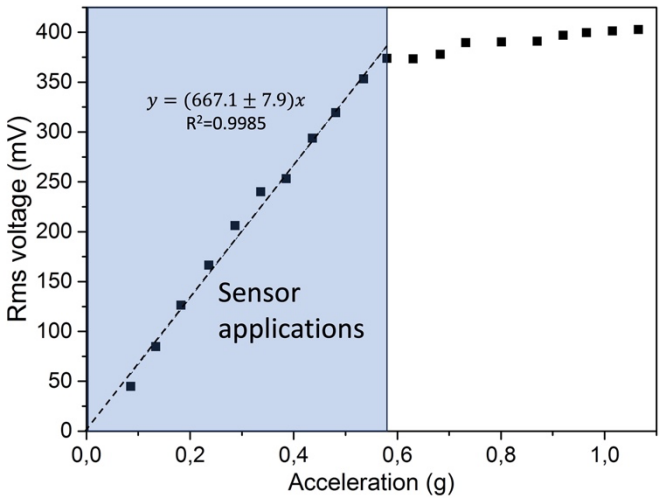

Figure 11. Voltage response of the $LiNbO_3$-Si cantilever (B cantilever) with tip mass as a function of acceleration at resonance frequency of 817 Hz.

3 Discussion and concluding remarks

Wafer scale microfabrication of lead-free piezoelectric MEMS transducers, based on thick $LiNbO_3$ films, has been demonstrated. The main challenge of deep etching of thick $LiNbO_3$ films was overcome by developing the pulsed Ar/SF_6 etching, which enabled to etch $LiNbO_3$ thickness of 5 µm in one step with etching rate of 28 nm/min, which is similar to the rate attained by physical etching, used for sub-micron $LiNbO_3$ structures [16].

The resonance frequency of $LiNbO_3$-Si cantilever with the total area of 4.02 mm^2 (dimensions of 6.7 x 0.6 x 0.042 mm^3) was 511 Hz, which is in the range of low frequencies attained for the piezoelectric MEMS scale (devices with surface area < 10 mm^2). For example, for the resonance frequency of PZT-Si and AlN-Si cantilevers with tip mass and the area of 0.32 mm^2/2.5 mm^2 and 2.25 mm^2 were 870 Hz/2300Hz [41,42] and 1041 Hz [43], respectively. In the MEMs scale piezoelectric transducers, one of the lowest resonance frequency of 20-30 Hz was attained by using the cantilevers based on thin-film silicon and parylene substrates [44] but with very big tip mass.

The electromechanical coupling of 5%, measured for the $LiNbO_3$-Si cantilevers, presents an improvement with respect to previously reported value of 0.7% for (YXlt)/163°/90°$LiNbO_3$-Si cantilever [45]. The electromechanical coupling of 14.8 % was reported for the transducer based on 20µm thick PZT [2]. The comparison of geometrical parameters of these devices and their resonant frequencies in line with electromechanical coupling is given in Table 1. Considering that (YXlt)/128°/90°$LiNbO_3$ and PZT present similar material coupling for actuation and mechanical energy harvesting [8], further optimization of geometrical

parameters is needed to further maximise the performance of the electro-active MEMS based on $LiNbO_3$.

Table 1 Comparison of dimensions (length x width x thickness in mm), resonance frequency, f_r, and K^2 for cantilevers based on piezoelectric films.

Material stack	Dimensions	Mass tip	f_r, Hz	K^2, %
(YXlt)/163°/90° $LiNbO_3$-Si [45]	6.5x0.8x0.12	No	4096	0.7
(YXlt)/128°/90° $LiNbO_3$-Si	6.7x0.6x0.041	(2x0.6x0.5)	511	4.8
Ni/PZT-Si [2]	5.75x10.8x0.05	Si 5.75x10.8x0.5 Ni 5.75x10.8x0.17	91	14.8

The capacitance of the studied $LiNbO_3$-Si MEMS transducer was 0.25 nF while the capacitance in the range of 1 nF is required for the energy harvesting applications. In the case of vibrational energy harvesting applications, further optimization of geometrical parameters is needed to bring the resonance frequency below the 100 Hz and to increase the impedance of the transducer in order to attain impedance matching with the harvesting circuit and to increase the harvested power level. However, the main application fields of electro-active MEMS are actuators and sensors. The fabricated MEMS, based on $LiNbO_3$ thick layers, have demonstrated highly linear displacement with good sensitivity (5.28 ± 0.02 µm/V) as a function of applied voltage indicating a suitability of the structure for actuation purposes. Moreover, the voltage response of 667 mV/g might be considered for acceleration or frequency sensing with high precision.

Acknowledgements

This work was conducted under the MSCA-ITN-2016 ENHANCE Project (H2020 MSCA-ITN Enhance project grant agreement No 722496), which is supported by the European Community under the Horizon 2020 Program. This was supported also by French RENATECH network and its FEMTO-ST technological facility, Bourgogne Franche-Comté region, the French national ANR projects FIESTA ANR-20-CE05-0026, and the graduate school EUR EIPHI contract ANR-17-EURE-0002. Authors are grateful to Thanks to PLASMA-THERM Europe for their help and advice on the various tests that were carried out on the RIE machine "Corial 200R-109".

Data availability statement

The data that support the findings of this study are available upon reasonable request from the authors.

References

[1] Toshiyoshi H, Ju S, Honma H, Ji C-H and Fujita H 2019 *Science and Technology of Advanced Materials* **20** 124–43
[2] Janphuang P, Lockhart R, Uffer N, Briand D and de Rooij N.F 2014 *Sensors and Actuators A: Physical* **210** 1-9
[3] Bartasyte A, Clementi G, Micard Q, Labbaveettil I, Moreira A-S-L, Boujnah S, Ouhabaz M, Verma A, Malandrino G, Mathur S, Dulmet B and Margueron S 2023 *J. Micromechanics and Microengineering* **33** 053001
[4] Kanno I, Ouyang J, Akedo J, Yoshimura T, Malic B and Muralt P 2023 *Appl. Phys. Lett.* **122** 090401
[5] Shibata K, Watanabe K, Kuroda T and Osada T 2022 *Appl. Phys. Lett.* **121** 092901
[6] Bartasyte A, Margueron S, Baron T, Oliveri S and Boulet P 2017 *Adv. Mater. Interfaces* **4** 1600998
[7] Gong S, Song Y-H, Manzaneque T, Lu R, Yang Y and Kourani A 2017 *IEEE 60th International Midwest Symposium on Circuits and Systems (MWSCAS)* 45-48
[8] Clementi G, Ouhabaz M, Margueron S, Suarez M-A, Bassignot F, Gauthier-Manuel L, Belharet D, Dulmet B and Bartasyte A 2021 *Appl. Phys. Lett.* **119** 013904
[9] Solal M, Pastureaud T, Ballandras S, Aspar B, Biasse B, Daniau W and Hode J-M 2002 *IEEE Ultrasonics Symposium* **1** 131-134
[10] Pastureaud T, Solal M, Biasse B, Aspar B, Briot J-B, Daniau W, Steichen W, Raphael L, Laude V, Laëns A, Friedt J-M and Ballandras S 2007 *IEEE Transactions on Ultrasonics, Ferroelectrics, and Frequency Control* **54** 870-876
[11] Clementi G, Lombardi G, Margueron S, Suarez M-A, Lebrasseur E, Ballandras S, Imbaud J, Lardet-Vieudrin F, Gauthier-Manuel L, Dulmet B, Lallart M and Bartasyte A 2021 *Mechanical Systems and Signal Processing* **149** 107171
[12] Gong S 2017 *Piezoelectric MEMS Resonators* 99-129
[13] Zhuang R, He J and Li Y 2023 *Adv. Mater.* **35** 2208113
[14] Hui H, Ricken R and Sohler W 2008 *ECIO, Eindhoven*
[15] Randles A-B, Esashi M and Tanaka S 2010 *IEEE Transactions on Ultrasonics, Ferroelectrics, and Frequency Control* **57** 2372 – 2380
[16] Wang C, Burek M-J, Lin Z, Atikian H-A, Venkataraman V, Huang I-C, Stark P, and Lončar M 2014 *Opt. Express* **22** 30924–30933
[17] Aryal A, Stricklin L, Behzadirad M, Branch D.W, Siddiqui A, Busani T 2022 *Nanomaterials*, **12**, 2836
[18] Banna S, Agarwal A, Tokashiki K, Cho H, Rauf S, Todorow V, Ramaswamy K, Collins K, Stout P, Lee J-Y, Yoon J, Shin K, Choi S-J, Cho H-S, Kim H-J, Lee C and Lymberopoulos D 2009 *IEEE Transactions on Plasma Science* **37** 1730-1746
[19] Boswell R-W and Henry D 1985 *Appl. Phys. Lett.* **47** 1095–1097
[20] Kanakasabapathy S-K, Overzet L-J, Midha V and Economou D 2001 *Appl. Phys. Lett.* **78** 22–24
[21] Verdeyen J-T, Beberman J and Overzet L 1990 *Journal of Vacuum Science & Technology A: Vacuum, Surfaces, and Films* **8** 1851–1856
[22] Ahn T-H, Nakamura K and Sugai H 1996 *Plasma Sources Science and Technology* **5** 139

[23] Hwang G-S and Giapis K-P 1998 *Japanese journal of applied physics* **37** 2291
[24] Samukawa S, Noguchi K, Colonell J-I, Bogart K-H, Malyshev M-V and Donnelly V-M 2000 *Journal of Vacuum Science & Technology B: Microelectronics and Nanometer Structures Processing, Measurement, and Phenomena* **18** 834-840
[25] Petit-Etienne C, Darnon M, Vallier L, Pargon E, Cunge G, Boulard F, Joubert O, Banna S and Lill T 2010 *Journal of Vacuum Science & Technology B* **28** 926-934
[26] Petit-Etienne C, Pargon E, David S, Darnon M, Vallier L, Joubert O and Banna S 2012 *Journal of Vacuum Science & Technology B* **30** 040604
[27] Samukawa S and Mieno T 1996 *Plasma Sources Science and Technology* **5** 132
[28] Ohtake H, Noguchi K, Samukawa S, Iida H, Sato A and Qian X-Y 2000 *Journal of Vacuum Science & Technology B: Microelectronics and Nanometer Structures Processing, Measurement, and Phenomena* **18** 2495-2499
[29] Voronin S-A, Alexander M-R and Bradley J-W 2005 *Measurement Science and Technology* **16** 2446
[30] Samukawa S, Ishikawa Y, Kumagai S and Okigawa M 2001 *Japanese journal of applied physics* **40** L1346
[31] Okigawa M, Ishikawa Y and Samukawa S 2003 *Japanese Journal of Applied Physics **42*** 2444
[32] Cunge G, Vempaire D and Sadeghi N 2010 *Applied Physics Letters* **96** 131501
[33] Subramonium P and Kushner MJ 2004 *Journal of applied physics* **96** 82-93
[34] Ohtake H, Noguchi K, Samukawa S, Iida H, Sato A and Qian X-Y 2000 *Journal of Vacuum Science & Technology B: Microelectronics and Nanometer Structures Processing, Measurement, and Phenomena* **18** 2495-2499
[35] Franz Lärmer and Andrea Schilp: Patents DE 4241045, US. 5501893 and EP 625285
[36] Janet Hopkins, Ian Ronald Johnston & al: Patent US 6,187,685
[37] Huff M 2021 *Micromachines* **12** 991
[38] Balbi J-H, Duffaud J-A and Besson R-J 1978 In *32nd Annual Symposium on Frequency Control IEEE* 162-168
[39] Raj P-R and Santhosh B 2019 *International Journal of Mechanical Sciences* **152** 268-279
[40] Pang X and Yong Y-K 2019 *IEEE transactions on ultrasonics, ferroelectrics, and frequency control* **67** 422-430
[41] Muralt P, Marzencki M, Belgacem B, Calame F and Basrour S 2009 *Procedia Chemistry* **1** (1) 1191–1194
[42] Isarakorn D, Briand D, Janphuang P, Sambri A, Gariglio S, Triscone J M, Guy F, Reiner J W, Ahn C H and De Rooij N F 2011 *SmartMaterials and Structures* **20** 2
[43] Zhang J, Cao Z and Kuwano H 2011 *Japanese Journal of Applied Physics* **50** (9) 3
[44] Jackson N, Olszewski OZ, O'Murchu C and Mathewson A 2018 *J. Micro/nanolithography, MEMS, and MOEMS* **17** (1) 015005
[45] Barrientos G, Clementi G, Trigona C, Ouhabaz M, Gauthier-Manuel L, Belharet D, Margueron S, Bartasyte A, Malandrino G and Baglio S. *Sensors* **22** 559